Acoustic Far-Field Hypersonic Surface Wave Detection with Single Plasmonic Nanoantennas

Rodrigo Berte,[1,2,*] Fabricio Della Picca,[3,*] Martín Poblet,[3] Yi Li,[1] Emiliano Cortés,[1,4] Richard V. Craster,[5] Stefan A. Maier,[1,4,†] and Andrea V. Bragas[3,‡]

[1]*The Blackett Laboratory, Department of Physics, Imperial College London, London SW7 2AZ, United Kingdom*
[2]*CAPES Foundation, Ministry of Education of Brazil, Brasília, DF 70040-020, Brazil*
[3]*Departamento de Física, FCEN, IFIBA CONICET, Universidad de Buenos Aires, Intendente Güiraldes 2160, C1428EGA Buenos Aires, Argentina*
[4]*Chair in Hybrid Nanosystems, Nanoinstitut München, Fakultät für Physik, Ludwig-Maximilians-Universität München, 80799 München, Germany*
[5]*Department of Mathematics, Imperial College, London SW7 2AZ, United Kingdom*

(Received 16 August 2018; published 20 December 2018)

The optical properties of small metallic particles allow us to bridge the gap between the myriad of subdiffraction local phenomena and macroscopic optical elements. The optomechanical coupling between mechanical vibrations of Au nanoparticles and their optical response due to collective electronic oscillations leads to the emission and the detection of surface acoustic waves (SAWs) by single metallic nanoantennas. We take two Au nanoparticles, one acting as a source and the other as a receptor of SAWs and, even though these antennas are separated by distances orders of magnitude larger than the characteristic subnanometric displacements of vibrations, we probe the frequency content, wave speed, and amplitude decay of SAWs originating from the damping of coherent mechanical modes of the source. Two-color pump-probe experiments and numerical methods reveal the characteristic Rayleigh wave behavior of emitted SAWs, and show that the SAW-induced optical modulation of the receptor antenna allows us to accurately probe the frequency of the source, even when the eigenmodes of source and receptor are detuned.

DOI: 10.1103/PhysRevLett.121.253902

The ability of metallic nanostructures to confine light at subdiffraction volumes in their near field allows the local enhancement of inherently weak phenomena such as Raman scattering [1], infrared absorption [2], and higher harmonic generation [3]. The decay of these optical excitations, given the large absorption cross sections and fast electronic relaxation processes, makes nanostructured conducting materials efficient local transducers of far-field electromagnetic radiation into mechanical energy. In addition, the strong optical modulation provided by the launched coherent acoustic modes in these nanostructures allows their exploitation as exquisitely sensitive mechanical probes of their near environment. The efficient generation of acoustic waves by nanostructured transducers and the strong self-modulation provided by the launched coherent phononic modes have enabled their application as, for instance, light-source modulators [4], photoacoustic amplifiers [5], and mass sensors [6,7].

The spectrally narrow acoustic modes obtained in these nanostructures are defined by the resonator's constitution and multiple boundary conditions such as size, shape, composition, their substrate, and embedding media. This parameter space has been systematically explored where resonances were tuned by changes in adhesion layer thickness [8], mechanical constraints [9], by positioning resonators over trenches [10], and even by mode interference from a delayed two-pump excitation scheme [11]. Equally importantly, the damping of acoustic vibrations, which defines the spectral linewidth of modes, is a prominent aspect in the application of these systems, and has also received considerable attention, being successfully modeled for infinite isotropic environments [10,12–16]. However, the multiple decay mechanisms in environments without spherical or cylindrical symmetry, such as when particles lie on a substrate, remain poorly understood [17]. In these cases, to determine the damping and quality factors of resonances, current practice (Ref. [18]) is to use empirical fitting of the decaying modulated time-domain signals.

Among different contributions to the measured effective damping of a particular phononic mode, the radiation of acoustic waves to the embedding matrix or the substrate, is qualitatively assessed via the mismatch in acoustic impedance (Z) between the vibrating object and its environment. In the longitudinal plane wave limit the impedance is given by $Z = \rho_j c_{Lj}$ (being ρ_j the j medium density and c_{Lj} the corresponding longitudinal wave speed). However, such a qualitative analysis may be misleading as Z is a mode-dependent parameter, and for which low damping can be obtained even for a perfect impedance match [16]. Accordingly, theoretical calculations have systematically

predicted shorter acoustic damping times for particles in solid matrixes and longer damping times for liquid environments when compared to experimental values [18]. Nevertheless, the damping through the coupling of nanostructures to the substrate has been shown to lead to the emission of surface acoustic waves (SAWs) which have been successfully obtained in nanowires [17] and in periodic arrays of plasmonic nanoantennas [19–21]. The latter induce collective modes of the array and the substrate, allowing tailored dispersion defined by the periodicity of the lattice, and, more recently, pump polarization-controlled modes [22]. However, the use of periodic arrays has limitations such as the generation of pseudo-SAWs due to scattering into the substrate [21,23] and inhomogeneous damping caused by the size dispersion of nanostructures. Thus, measurements in single nanostructures are required to further elucidate the acoustic wave damping of the generated coherent phonons [24].

Although acoustic damping of particles on a substrate seems to be dominated by internal crystalline defects, as recently reported [25], in this Letter we report that vibrational modes in single nanostructures can significantly couple to SAWs on the underlying substrate and thereby probed in the acoustic far field. These SAW excitations induce coherent vibrations in a second nanoantenna at distances much larger than the characteristic amplitude of modes of the source, which are estimated to be on the order of subnanometric and even subatomic scales [26,27]. The choice of single antennas for generation and detection of SAWs avoids inhomogeneous damping due to size dispersion, which through destructive interference leads to underestimation for mode lifetimes. Distance-dependent detection times reveal mechanical properties of the substrate, such as surface wave speed, and finite-element method calculations suggest mode-dependent emission of Rayleigh and bulk shear waves. These emitted waves expose fundamental aspects of acoustic mode damping in nanostructures; the coupling of SAWs and plasmonic modes in single nanoantennas demonstrated here has potential to extend their range of applications from pure local transducers or self-modulated probes to sensitive mechanical sensors, such as in nondestructive fatigue cracks detection at the nanoscale. The goal of in-phase stimulated emission of acoustic phonons ultimately depends on the complete understanding of the coupling between transducers and a transport media, either a surrounding matrix or a substrate [28].

To study the generation and detection of SAWs, gold nanoantennas were fabricated on fused-silica substrate with a 2 nm chromium adhesion layer through standard electron-beam lithography, thermal evaporation, and lift-off techniques [9]. The amorphous fused silica was chosen as substrate due to its widespread use in nanofabrication, although a lower damping of SAWs is expected for crystalline substrates such as sapphire [29]. The role of different frequencies on the generation and propagation of SAWs was assessed by varying the geometry, in-plane dimensions, and distance between nanoantennas assigned as source (S) and receptor (R) of acoustic waves. Nondegenerate sub-ps delayed pump-probe pulses were used for the excitation of coherent phonons in the source via interband transitions at 405 nm wavelength and detection of SAWs through transient transmission of the probe due to acoustic modulation of localized surface plasmon resonances (LSPRs) of the receptor at 810 nm wavelength. The pump-probe experimental setup is depicted schematically in Fig. 1(a) where it is also shown, in a zoom of the sample zone, that the pump and probe beams can be independently directed through positioning adjustment stages to different points of the focal plane and thus be focusing on different antennas. Finite-element method (FEM) calculations, performed with the commercially available software Comsol Multiphysics (details in the Supplemental Material [30]), in the time-domain reveal the SAWs emission pattern, shown in Fig. 1(b), for a Au rod and a disk. Here, the displacive excitation mechanism was considered, corresponding to an exponential increase in the lattice temperature (T_L) as resulting from a two-temperature (electron-lattice) model $T_L(t) = T_0 + (T_{\mathrm{eq}} - T_0)[1 - \exp(-t/\tau^0_{e-L})]$, where $T_0 = 293.15$ K is the initial temperature, $T_{\mathrm{eq}} = 393.15$ K the estimated lattice equilibrium temperature, and τ^0_{e-L} the electron-lattice energy-transfer time ($\tau^0_{e-L} \approx 1.1$ ps for Au) [18]. Deviations from the exponential behavior, and slower lattice temperature increase, are expected for intense pump pulses, as the electronic heat capacity becomes dependent on the electron gas temperature. However, the employed relation should provide us a lower bound on the timescale of lattice heating. The emission pattern curves were obtained by averaging the far-field displacement in sequential 100 ps time intervals. Isotropic emission is obtained for a disk, as expected from its symmetry, shown in Fig. 1(b), only for the initial 0–100 ps interval for clarity, a pattern that is maintained for longer times. Conversely, the rod emission is highly anisotropic, being initially along its minor axis due to the larger contact area with the substrate and the initial expansion of the nanoparticle in all directions following the fast lattice heating. This is illustrated in Fig. 1(c), where the substrate displacement at $t = 50$ ps is shown.

The pattern then converges to an emission along the rod major axis, corresponding to the excitation of the SAWs emission pattern obtained for its main extensional mode, as shown in the Supplemental Material [30]. The experimental self-modulation, when pump and probe are set at the same particle, are shown in Fig. 1(d) for the rod (blue) and disk (red) nanoantennas. Oscillations corresponding to the rod extensional mode and to the disk in-plane radial (breathing) mode are observed, as revealed by the Fourier components of the modulated signal as compared with those of FEM calculations [Fig. 1(d)—inset]. Experimental frequencies (solid-square lines) are in both cases higher than the calculated ones (dashed-circle lines), a discrepancy

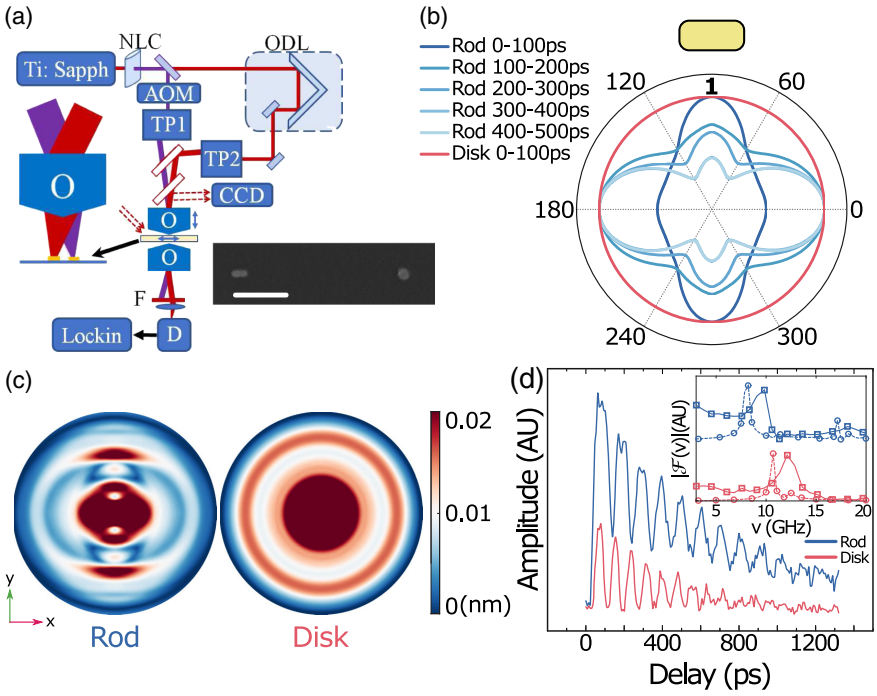

FIG. 1. (a) Schematic representation of pump-probe experiment. NLC: nonlinear crystal, ODL: optical delay line, AOM: acousto-optic modulator, O: microscope objective, D: photodetector, TP: telescope and position adjustment. (inset) SEM image of a rod source and a disk receptor 1.5 μm distant. Scale bar corresponds to 500 nm. (b) FEM average displacement at the edge of the simulation region of a $140 \times 60 \times 35$ nm rod (blue, 0–500 ps) and a 140×35 nm disk (red, 0–100 ps). Rod orientation is shown on top. (c) Substrate displacement at $t = 50$ ps. Antennas omitted for clarity. (d) Modulated probe transmission of single antennas. (inset) Fourier transform of probe signals (solid-square lines) and FEM size variations along x axis (dashed-circle lines).

attributed mainly to size deviations in the thickness of the nanoantennas from the nominal nanofabrication values used for calculations.

To test whether the emitted SAWs could be detected in the acoustic far field, a receptor nanoantenna was positioned at distances varying from 1–3 μm from the source. The distances between source and receptor were chosen in order to avoid the excitation of the receptor by the diffraction-limited pump beam while allowing for a significant mechanical excitation by the SAWs. Results of transient probe transmission for rod and disk receptors are shown in Figs. 2(a) and 2(b). A clear delay and reduction in amplitude of the transient signal is obtained for receptors positioned at larger distances from the source. The initial excitation or wave arrival time of each receptor is plotted in Fig. 2(c), with corresponding linear fits (black lines) for each receptor geometry. The fits allow direct determination of SAW speed, where 3400 ± 5 m/s and 3210 ± 14 m/s were obtained for the rod and disk receptors, respectively. Distances between nanofabricated source and receptor are set from center to center of the antennas, implying that the edge of the disks are nominally closer to the source than those of the rotated rod detectors by tens of nm; the contribution of this size difference only leads to small changes in the detection time, of a few ps for the average wave speed (3305 ± 15 m/s) of both detectors.

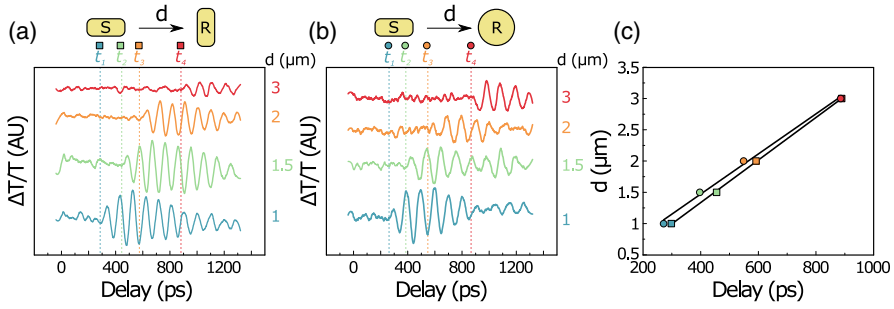

FIG. 2. Transient probe transmission for (a) a rod and (b) disk receptors (R) at varying distances (d) from the source (S). (c) SAW arrival time at varying distances with corresponding linear fits (black lines) for both receptor geometries.

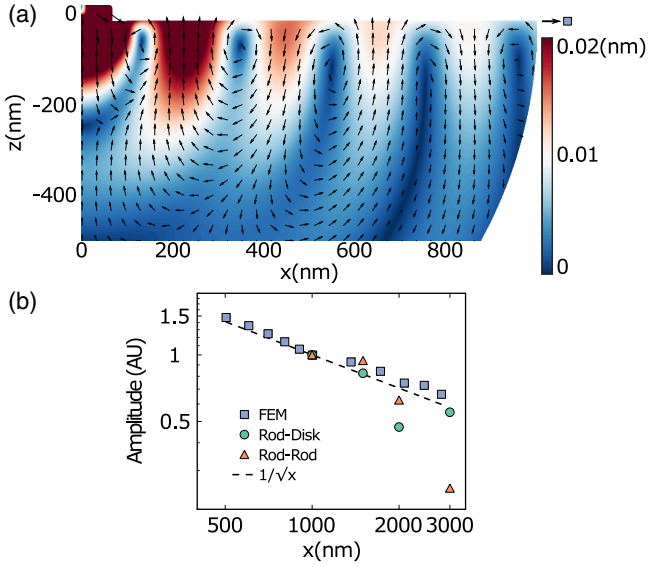

FIG. 3. (a) xz-plane cross section of displacement (color scale) and polarization (black arrows) of the extensional mode of a $140 \times 60 \times 35$ nm Au rod (top left of image) at 8.3 GHz. (b) Normalized amplitudes at 1 μm of the extensional mode displacement at the surface [grey squares indicated by arrow in (a)] and transient probe transmission for disk (green circles) and rod (orange triangles) receptors. Black dashed line shows the $d^{-0.5}$ expected decay behavior of a Rayleigh wave away from its source.

The obtained fit values are lower than the measured speed of bulk shear (transverse) waves (c_t) in fused silica, 3764 m/s [31]. Nevertheless, SAWs in deep semi-infinite linear elastic substrates, termed Rayleigh waves [32], have a propagating speed (c_R) smaller than that of their bulk transverse (shear) counterpart. For materials with a Poisson's ratio (ν) in the interval $0 \leq \nu \leq 0.5$ an accurate and often used [32,33] approximation to obtain c_R is $(c_R/c_t) = (0.87 + 1.12\nu)/(1 + \nu)$, that for fused silica ($\nu = 0.17$) gives $c_R = 3411$ m/s, corresponding to an $\approx$3.2% deviation from the average value (3305 ± 15 m/s) of experimental fits. The measured amplitudes were then compared with that of the main rod extensional mode obtained from FEM calculations in the frequency domain, whose substrate field amplitude and polarization are shown in Fig. 3(a). Notably, the characteristic elliptical polarization of Rayleigh waves, comprising longitudinal and transverse excitations, is observed [34].

A distinct difference from the rod extensional mode is observed for the rod breathinglike and the disk in-plane radial modes, where a significant emission of bulk shear waves occurs, as shown in the Supplemental Material [30]. To compare the calculated mechanical amplitudes with those of probe differential transmission, both values were normalized at a distance of 1 μm from the source, corresponding to the position of the closest receptor. FEM calculations in Fig. 3(b) show excellent qualitative agreement with the $d^{-0.5}$ scaling (black dashed line) expected for the decay of a Rayleigh wave away from its source [32]. We attribute the small discrepancy to the finite size of the source, as higher order multipoles can contribute to the emission of SAWs, and to diffraction of the transverse S waves emitted into the substrate. Experimental amplitudes for both rod and disk receptors also show this decay behavior when positioned at larger distances from the source, again with relatively good agreement to the ideal Rayleigh wave. The lower amplitudes at the largest distances, observed experimentally, suggest additional damping of the SAWs as they propagate on the substrate due to scattering at imperfections and thermoelastic effects, the latter being negligible for fused silica at lower frequencies [35], and which were not considered in our calculations. In addition, the small size dispersion of the receptors should lead to appreciable differences in the spectral position of the probe laser relative to their LSPR, being ideally positioned at the half-maximum of the plasmonic resonance. This would imply non-negligible variation in probe modulation amplitude. Nevertheless, the observed trend in reduced amplitude with distance is still evident.

Finally, the spectral content of the probe differential transmission measured on the receptor and its comparison to the time-domain numerical results are shown in Fig. 4. It is important to note here again that these signals are generated by the mechanical excitation of the receptor nanoantenna by SAWs, different from the usual optical excitation in these types of experiments, like the one shown in Fig. 1(d). This scenario leads to the conclusion that the symmetry of the excited modes must correspond to the excitation of a wave arriving from one side, different from that one produced by the transfer of energy of an excited plasmon or interband transition onto the mechanical degrees of freedom of the nanoantenna. The experiments and numerical calculations shown in Fig. 4 were performed with a rod as a source, and using a rod or a disk as receptors, establishing identical values that vary between 100 nm (fainter colors) and 140 nm (stronger colors) for the length of the main axis of the rods and for the diameter of the disk. In Fig. 4 red empty circles show the frequency values for the optically excited modes on the receptor nanoantennas, similar to that performed in experiments shown in Fig. 1(d). For the case of using a rod as a receptor, Fig. 4(a)—top panel, the frequencies in the SAW signals on the receptor (blue squares) are identical to those emitted by the source (green triangles) and those optically induced in the receptors (red circles). However, in the case of the disk as a receptor, the SAW mechanical excitation matches the source frequency whereas the main radial symmetric mode (lying at higher frequencies) is not efficiently excited in the receptor. Indeed, we have seen in these experiments that the detection of SAWs signals with disks is, in general, less sensitive than with rods. All this is confirmed by the FEM time-domain simulations shown in Fig. 4(b), that were performed by positioning receptors at a distance of 1 μm

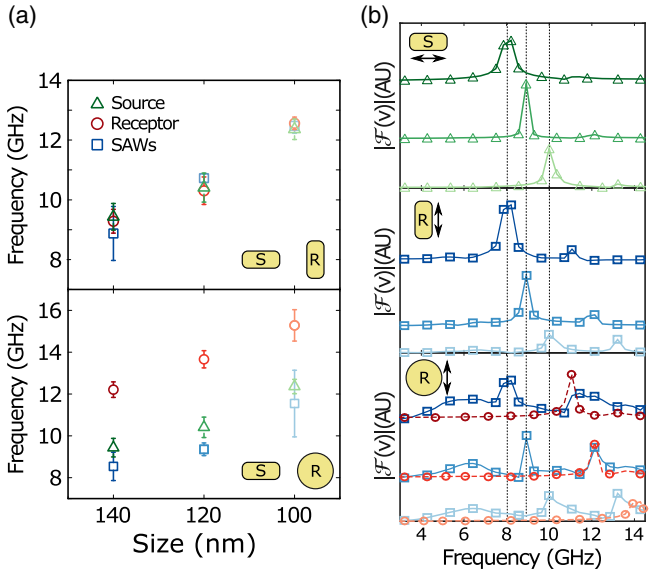

FIG. 4. (a) Averaged experimental frequencies of rod sources (60 nm width, 30 nm height—green triangles), and rod (60 nm width, 30 nm height, top) or disk (30 nm height, bottom) receptors (R—red circles) of indicated main-axis size (diameter for disks). Stronger colors correspond to larger sizes. Blue squares indicate the measured SAW-induced probe modulation frequencies at the receptor when the pump beam is set at the source. (b) FEM time-domain Fourier components of the size variation along the axes parallel to the probe beam polarization (black arrows) for the rod source (top), and rod (middle), and disk (bottom) receptors. Vertical dashed lines correspond to extensional modes of the sources. Disk radial modes are shown in red dashed lines and circles (bottom).

from the source nanoantennas, in the same configurations as shown in Fig. 2. Here, the Fourier components of the time-domain size variations of source and receptor axes parallel to the probe polarization used in experiments (black arrows) were analyzed. Results show that SAWs generated by the source (top) induce variations in the size of the rod (middle) and disk (bottom) receptors at the same frequency of the main extensional mode of the source (dashed vertical lines). The frequency of the source is also shown to be detuned from the radial mode of the disk (bottom, red dashed line and circles), which is not excited as efficiently as size variations at the source frequency. For the case of rod sources and receptors of nonidentical sizes, numerical calculations predict that SAWs excite the detuned receptor modes as efficiently as the frequencies of the source, here attributed to the spectral proximity and identical displacement profiles of the extensional modes (see Supplemental Material [30]).

In conclusion, SAWs emitted by single plasmonic nanoantennas in the acoustic far field modulate the optical response of a second nanostructure by mechanically exciting it through the substrate. The emitted waves show the characteristic propagation velocities and amplitude decay akin to Rayleigh waves in semi-infinite elastic substrates, as investigated experimentally by pump-probe techniques and with FEM calculations. The 2 nm chromium layer used here should not provide a full adhesion to the fused-silica substrate [8], although enough to allow a stable attachment of the nanoparticles. As the emission of acoustic waves has been demonstrated for Cooper nanowires on silicon substrates without an adhesion layer [17], further studies are needed to address the possibility of the generation and detection of SAWs by chemically synthesized particles. Colloidal particles possess much higher Q factors and they could be positioned over substrates without adhesion layers through, for example, optical printing [36]. The generation of SAWs is a fundamental aspect of the fast decay of electronic excitations in nanostructures and subsequent damping of generated coherent phonons. The detection in the far field of these minute vibrations shows the exquisite sensitivity of the optical response of plasmonic nanostructures to mechanical excitations, revealing properties of the substrate in the hypersonic regime and extending the application of nanoantennas as local transducers and self-modulated probes. We envisage applications such as the nondestructive detection of fatigue cracks at the nanoscale and the measurement of mechanical properties of small flakes of 2D materials, that are usually limited in lateral size due to fabrication constraints of growth and exfoliation techniques.

R. B. acknowledges the Capes Foundation for a Science Without Borders fellowship (Bolsista da Capes–Proc. No. BEX 13.298/13-5). R. V. C. and S. A. M acknowledge the EPSRC EP/L024926/1, and S. A. M the Lee-Lucas Chair in Physics. This work was partially supported by PIP 112 201301 00619, UBACyT Proyecto 20020130100775BA. R. V. C. and S. A. M. acknowledge funding from Air Force Office of Scientific Research/EOARD (FA9550-17-1-0300). R. V. C. thanks the Leverhulme Trust for a Research Fellowship.

*R. B. and F. D. P. contributed equally to this work.
†Stefan.Maier@physik.uni-muenchen.de
‡bragas@df.uba.ar

[1] M. Fleischmann, P. J. Hendra, and A. J. McQuillan, Chem. Phys. Lett. **26**, 163 (1974).
[2] A. Hartstein, J. R. Kirtley, and J. C. Tsang, Phys. Rev. Lett. **45**, 201 (1980).
[3] C. K. Chen, A. R. B. de Castro, and Y. R. Shen, Phys. Rev. Lett. **46**, 145 (1981).
[4] C. Brüggemann, A. V. Akimov, A. V. Scherbakov, M. Bombeck, C. Schneider, S. Höfling, A. Forchel, D. R. Yakovlev, and M. Bayer, Nat. Photonics **6**, 30 (2012).
[5] Y. S. Chen, W. Frey, S. Kim, P. Kruizinga, K. Homan, and S. Emelianov, Nano Lett. **11**, 348 (2011).
[6] K. Y. Fong, M. Poot, and H. X. Tang, Nano Lett. **15**, 6116 (2015).
[7] K. Yu, J. E. Sader, P. Zijlstra, M. Hong, Q.-H. Xu, and M. Orrit, Nano Lett. **14**, 915 (2014).

[8] W. S. Chang, F. Wen, D. Chakraborty, M. N. Su, Y. Zhang, B. Shuang, P. Nordlander, J. E. Sader, N. J. Halas, and S. Link, Nat. Commun. **6**, 7022 (2015).
[9] F. Della Picca, R. Berte, M. Rahmani, P. Albella, J. M. Bujjamer, M. Poblet, E. Cortés, S. A. Maier, and A. V. Bragas, Nano Lett. **16**, 1428 (2016).
[10] T. A. Major, A. Crut, B. Gao, S. S. Lo, N. D. Fatti, F. Vallée, and G. V. Hartland, Phys. Chem. Chem. Phys. **15**, 4169 (2013).
[11] K. O'Brien, N. D. Lanzillotti-Kimura, J. Rho, H. Suchowski, X. Yin, and X. Zhang, Nat. Commun. **5**, 4042 (2014).
[12] L. Saviot, C. H. Netting, and D. B. Murray, J. Phys. Chem. B **111**, 7457 (2007).
[13] M. Pelton, J. E. Sader, J. Burgin, M. Liu, P. Guyot-Sionnest, and D. Gosztola, Nat. Nanotechnol. **4**, 492 (2009).
[14] C. C. Hsueh, R. Gordon, and J. Rottler, Nano Lett. **18**, 773 (2018).
[15] N. Del Fatti, C. Voisin, F. Chevy, F. Vallée, and C. Flytzanis, J. Chem. Phys. **110**, 11484 (1999).
[16] L. Saviot and D. B. Murray, Phys. Rev. Lett. **93**, 055506 (2004).
[17] C. Jean, L. Belliard, T. W. Cornelius, O. Thomas, Y. Pennec, M. Cassinelli, M. E. Toimil-Molares, and B. Perrin, Nano Lett. **16**, 6592 (2016).
[18] A. Crut, P. Maioli, N. Del Fatti, and F. Vallée, Phys. Rep. **549**, 1 (2015).
[19] J. F. Robillard, A. Devos, and I. Roch-Jeune, Phys. Rev. B **76**, 092301 (2007).
[20] C. Giannetti, B. Revaz, F. Banfi, M. Montagnese, G. Ferrini, F. Cilento, S. Maccalli, P. Vavassori, G. Oliviero, E. Bontempi, L. E. Depero, V. Metlushko, and F. Parmigiani, Phys. Rev. B **76**, 125413 (2007).
[21] D. Nardi, M. Travagliati, M. E. Siemens, Q. Li, M. M. Murnane, H. C. Kapteyn, G. Ferrini, F. Parmigiani, and F. Banfi, Nano Lett. **11**, 4126 (2011).
[22] N. D. Lanzillotti-Kimura, K. P. O'Brien, J. Rho, H. Suchowski, X. Yin, and X. Zhang, Phys. Rev. B **97**, 235403 (2018).
[23] H. N. Lin, H. J. Maris, L. B. Freund, K. Y. Lee, H. Luhn, and D. P. Kern, J. Appl. Phys. **73**, 37 (1993).
[24] R. Marty, A. Arbouet, C. Girard, A. Mlayah, V. Paillard, V. K. Lin, S. L. Teo, and S. Tripathy, Nano Lett. **11**, 3301 (2011).
[25] C. Yi, M. N. Su, P. Dongare, D. Chakraborty, Y. Y. Cai, D. M. Marolf, R. N. Kress, B. Ostovar, L. J. Tauzin, F. Wen, W. S. Chang, M. Jones, J. E. Sader, N. J. Halas, and S. Link, Nano Lett. **18**, 3494 (2018).
[26] G. Soavi, I. Tempra, M. F. Pantano, A. Cattoni, S. Collin, P. Biagioni, N. M. Pugno, and G. Cerullo, ACS Nano **10**, 2251 (2016).
[27] A. Ahmed, M. Pelton, and J. R. Guest, ACS Nano **11**, 9360 (2017).
[28] I. S. Grudinin, H. Lee, O. Painter, and K. J. Vahala, Phys. Rev. Lett. **104**, 083901 (2010).
[29] R. Weigel, D. P. Morgan, J. M. Owens, A. Ballato, K. M. Lakin, K.-Y. Hashimoto, and C. C. Ruppel, IEEE Trans. Microwave Theory Tech. **50**, 738 (2002).
[30] See Supplemental Material at http://link.aps.org/supplemental/10.1103/PhysRevLett.121.253902 for details on FEM calculations, far-field emission pattern, and source size variation numerical results.
[31] W. M. Haynes, *CRC Handbook of Chemistry and Physics* (CRC Press, Boca Raton, 2017).
[32] I. A. Viktorov, *Rayleigh and Lamb Waves—Physical Theory and Applications*, 1st ed. (Springer, New York, 1967).
[33] M. Rahman and T. Michelitsch, Wave Motion **43**, 272 (2006).
[34] V. Laude, *Phononic Crystals: Artificial Crystals for Sonic, Acoustic, and Elastic Waves* (De Gruyter Studies in Mathematical Physics, Berlin, 2015).
[35] S. D. Penn, G. M. Harry, A. M. Gretarsson, S. E. Kittelberger, P. R. Saulson, J. J. Schiller, J. R. Smith, and S. O. Swords, Rev. Sci. Instrum. **72**, 3670 (2001).
[36] J. Gargiulo, I. L. Violi, S. Cerrota, L. Chvátal, E. Cortés, E. M. Perassi, F. Diaz, P. Zemánek, and F. D. Stefani, ACS Nano **11**, 9678 (2017).